

Giant Magnetochiral Anisotropy in Weyl-semimetal WTe₂ Induced by Diverging Berry Curvature

Tomoyuki Yokouchi^{1†}, Yuya Ikeda², Takahiro Morimoto², and Yuki Shiomi¹

¹*Department of Basic Science, The University of Tokyo, Tokyo 152-8902, Japan*

²*Department of Applied Physics, The University of Tokyo, Tokyo 113-8656, Japan*

[†] To whom correspondence should be addressed. E-mail: yokouchi@g.ecc.u-tokyo.ac.jp

Abstract

The concept of Berry curvature is essential for various transport phenomena. However, an effect of the Berry curvature on magnetochiral anisotropy, i.e. nonreciprocal magneto-transport, is still elusive. Here, we report the Berry curvature originates the large magnetochiral anisotropy. In Weyl-semimetal WTe₂, we observed the strong enhancement of the magnetochiral anisotropy when the Fermi level is located near the Weyl points. Notably, the maximal figure of merit $\bar{\gamma}$ reaches $1.2 \times 10^{-6} \text{ m}^2 \text{ T}^{-1} \text{ A}^{-1}$, which is the largest ever reported in bulk materials. Our semiclassical calculation shows that the diverging Berry curvature at the Weyl points strongly enhances the magnetochiral anisotropy.

Whether physical responses are allowed or prohibited is closely related to symmetries [1]. For example, in the linear response regime, the anomalous Hall effect is allowed when time reversal symmetry is broken [2]. In contrast, spin Hall effect is allowed independent of both time reversal and crystalline symmetries [2]. In the nonlinear response regime, a nonlinear Hall effect without external magnetic field is allowed in a bilayer WTe_2 but prohibited in a bulk WTe_2 due to the difference in the crystalline symmetries between them [3,4]. In addition, the bulk photovoltaic effect, a nonlinear optical phenomenon, is allowed in system without spatial inversion symmetry [4, 5, 6]. Beyond the symmetry argument, the microscopic mechanisms of these physical phenomena have been intensively studied. An important finding is that the notion of the Berry curvature of electronic wave function is essential for the description of these phenomena [8]. For example, the intrinsic anomalous and spin Hall effects are proportional to the integral of Berry curvature over the Fermi sea [2]. In addition, recently, it is found that the Berry curvature also manifests itself in nonlinear responses; the nonlinear Hall effect under time reversal symmetry is induced by the dipole moment of the Berry curvature [3,4,9,10]. In one of the microscopic mechanisms of the bulk photovoltaic effect (shift current mechanism), photocurrent is quantified by the difference in the Berry connection between valance and conduction bands [11, 12]. Hence, investigating relationship between the Berry curvature and a physical response has been one of the central issues in modern condensed matter physics.

Only when the time reversal and spatial inversion symmetries are simultaneously broken, another class of the nonlinear responses is allowed, that is the magnetochiral anisotropy effect [13, 14, 15, 16, 17, 18, 19, 20, 21, 22, 23, 24, 25, 26, 27, 28, 29, 30, 31] which we focus on here. The magnetochiral anisotropy effect (also called the nonreciprocal magneto-transport effect) is nonreciprocal transport responses triggered by an external magnetic field; under magnetic fields, the longitudinal and transverse resistivity of a material is different for electric current I flowing to the right ($+I$) and to the left ($-I$). The magnetochiral anisotropy effect essentially differs from the nonlinear Hall effect, since the former requires time-reversal symmetry breaking but the latter does not. Hence physical

mechanisms different from the nonlinear Hall effect must exist in the magnetochiral anisotropy effect. So far several underlying mechanisms of the magnetochiral anisotropy effect have been clarified. For example, an asymmetric electron scattering [18, 19, 22, 23, 31] and the magnetic-field-induced deformation of the Fermi surface caused by the Zeeman term [17, 20] have been identified as the microscopic mechanisms. From the viewpoint of symmetry, modification of electron motion due to the Berry curvature is also expected to affect the magnetochiral anisotropy effect, since the momentum-integrated Berry curvature can be nonzero in systems with broken time-reversal symmetry. However, the role of the Berry curvature on the magnetochiral anisotropy effect has not been well explored.

To study the effect of Berry curvature on the magnetochiral anisotropy effect, Weyl semimetals with broken spatial inversion symmetry [32, 33] are a suitable candidate. Weyl semimetals are quantum materials characterized by topologically nontrivial band structure and possess pairs of band crossing points termed Weyl points. The Weyl points act as monopoles of the Berry curvature, and the Berry curvature becomes singular and diverges at the Weyl points. Hence, when the Fermi level is located near the Weyl points, the effect of the Berry curvature is maximized and thus the magnetochiral anisotropy effect is expected to be dramatically enhanced. In this paper, we demonstrate this scenario using bulk crystals of a polar Weyl semimetal WTe_2 . The symmetry of bulk WTe_2 is a $Pmn2_1$ (polar), and WTe_2 possesses four pairs of Weyl points [34,35,36]. Around the Weyl points, the Berry curvature is strongly enhanced as schematically shown in Fig. 1(a).

Generally, the direction of the electric field generated in the magnetochiral anisotropy effect depends on the magnetic field direction [13]. The presence of the mirror plane in WTe_2 constrains the expected direction of the voltage drop induced by the magnetochiral anisotropy responses in WTe_2 as shown in Figs. 1(b) and (c); the longitudinal response (hereafter called nonreciprocal magnetoresistance) is proportional to $\sin\theta$ and largest when the magnetic field (H) is perpendicular to the current. Here, θ is the relative angle between the magnetic-field direction and the current direction. In contrast, the transverse response (hereafter called second-harmonic Hall effect) is proportional to $\cos\theta$ and largest

when H is parallel to the current. Here, we note although the nonreciprocal magnetoresistance was reported in nanometre-thick WTe₂ whose Fermi level is apart from the Weyl points [20], both the nonreciprocal magnetoresistance and the second-harmonic Hall effect have not been well investigated when the Fermi level is tuned near the Weyl points hosting diverging Berry curvature.

In Figs. 1(d) and (e), we present the magnetic-field dependence of the second-harmonic Hall effect and the nonreciprocal magnetoresistance in bulk WTe₂ whose Fermi level is close to the Weyl points (sample F). Here, we evaluate the Fermi level position from the carrier densities of electrons and holes obtained by the Hall resistivity measurement (see [37] for details). Because the magnetochiral anisotropy effect is proportional to the magnitude of the square of the current density j^2 , we measured the second harmonic longitudinal and transverse resistivity (ρ_{xx}^{2f} and ρ_{yx}^{2f}) (see also [37] for details). In accord with the expected contribution from the magnetochiral anisotropy effect, the field profiles of ρ_{xx}^{2f} and ρ_{yx}^{2f} are anti-symmetric against the magnetic field. Here, ρ_{xx}^{2f} and ρ_{yx}^{2f} are anti-symmetrized with respect to the magnetic field (see also [37]). The field profiles of the nonreciprocal magnetoresistance and the second-harmonic Hall effect before anti-symmetrization [$\rho_{xx,\text{meas.}}^{2f}(H)$ and $\rho_{yx,\text{meas.}}^{2f}(H)$] is also anti-symmetric against the magnetic field as shown in Fig. S5 [37]. The figures of merit of the second-harmonic Hall effect $\bar{\gamma}_{yx} = 2\rho_{yx}^{2f}/(\rho_{xx}jB)$ and nonreciprocal magnetoresistance $\bar{\gamma}_{xx} = 2\rho_{xx}^{2f}/(\rho_{xx}jB)$ are as large as $1.2 \times 10^{-6} \text{ m}^2\text{T}^{-1}\text{A}^{-1}$ and $0.34 \times 10^{-6} \text{ m}^2\text{T}^{-1}\text{A}^{-1}$ at 1 T, respectively. Remarkably, $\bar{\gamma}_{yx}$ is approximately 3 times larger than the previously reported largest value of the magnetochiral anisotropy effect in ZrTe₅ [29]. Interestingly, the second-harmonic Hall effect (i.e. ρ_{yx}^{2f} for $H // I$) is larger than the nonreciprocal magnetoresistance (i.e. ρ_{xx}^{2f} for $H \perp I$) [Figs. 1(d) and (e)]. This feature cannot be explained by the previously reported asymmetric electron scattering mechanism, in which the magnitude of the second-harmonic Hall effect and the nonreciprocal magnetoresistance must be the same [19]. As will be discussed later, this difference originates from the effects of the Berry curvature and the chiral anomaly.

To further confirm that the observed signals originate from the magnetochiral anisotropy effect, first,

we investigated the dependence of ρ_{yx}^{2f} with $H//I$ on the input-current frequency (f) and on the current density (j) in sample A. The Fermi level of sample A is also located near the Weyl points as in sample F. As expected in the second-harmonic Hall effect, the magnitude of ρ_{yx}^{2f} is independent of f and linearly increases with increasing j in the low current density region [Figs. 2(a) and (b)]. Note that the deviation from the linear relationship in Fig. 2(b) at high current is attributed to the temperature increase due to the Joule heating effect; the maximum temperature increase is estimated to be approximately 2 K from the change in the linear longitudinal resistivity. Then, we investigated polarity-direction dependence; the sign of the second-harmonic Hall effect and the nonreciprocal magnetoresistance should be reversed when the polarity direction is reversed [13]. We divided a WTe₂ sample into two (samples D and L) so that the polarity directions are opposite to each other [Fig. 2(c)]. As shown in Figs. 2(d)-(g), the signs of ρ_{yx}^{2f}/ρ_{xx} and ρ_{xx}^{2f}/ρ_{xx} are opposite for samples D and L in accord with the expected trends in the second-harmonic Hall effect and the nonreciprocal magnetoresistance. We also measured ρ_{yx}^{2f}/ρ_{xx} as a function of the relative angle (θ) between the magnetic-field direction and the current direction. As shown in Fig. 3(a), ρ_{yx}^{2f}/ρ_{xx} obeys $\cos\theta$ as expected. These results corroborate that the observed signals originate from the magnetochiral anisotropy effect.

Then, we investigate the temperature dependence of the second-harmonic Hall effect and the nonreciprocal magnetoresistance. In Figs. 3(b) and (c), we show the temperature dependence of ρ_{yx}^{2f}/ρ_{xx} and ρ_{xx}^{2f}/ρ_{xx} at 9 T for sample A and sample F. As can be seen from Figs. 3(b) and (c), the absolute values of ρ_{yx}^{2f}/ρ_{xx} and ρ_{xx}^{2f}/ρ_{xx} increase notably with decreasing temperature. The enhancement at low temperatures should be closely related to the microscopic mechanism and will be discussed later.

Next, we investigated the Fermi level dependence of the second-harmonic Hall effect and the nonreciprocal magnetoresistance. In WTe₂, it is known that the Fermi level position changes due to a deficiency of Te and can be evaluated by the ratio between the hole carrier density (n_h) and the electron

carrier density (n_e) [38]. According to the previous study [38], when the Fermi level is close to the Weyl points, n_e/n_h is approximately 1.08. Hence, we measured $\bar{\gamma}_{yx}$ and $\bar{\gamma}_{xx}$ in more than ten samples and plot the absolute value of $\bar{\gamma}_{yx}$ and $\bar{\gamma}_{xx}$ at 1 T as a function of n_e/n_h (see also [37] for the evaluation of n_e and n_h). As shown in Figs. 4(a) and (b), $|\bar{\gamma}_{yx}|$ and $|\bar{\gamma}_{xx}|$ systematically depend on n_e/n_h or equivalently the Fermi level position. Notably, both $|\bar{\gamma}_{yx}|$ and $|\bar{\gamma}_{xx}|$ change by more than four orders of magnitude and are largest when the Fermi level is close to the Weyl points. The observed substantial increase in the magnetochiral anisotropy responses around the Weyl points cannot be explained by the previously reported semiclassical calculation of the nonreciprocal responses in WTe₂ [20], in which an effect of the Berry curvature is not included; in this previous work, the ratio of the change in the calculated nonreciprocal response is less than 10 as a function of the Fermi level position.

The observed Fermi-level dependence of the magnetochiral anisotropy effect can be understood by a semiclassical treatment of current responses including the contribution from the Berry curvature. We use Boltzmann equation to derive momentum distribution under the electric field and the magnetic field and calculate the second-harmonic Hall and nonreciprocal magnetoresistance responses (for detail, see [37]). We find that the combination of C_2 rotation symmetry of WTe₂ around the z direction and the time reversal symmetry leads to a constraint that the transverse nonreciprocity ρ_{yx}^{2f} and longitudinal nonreciprocity ρ_{xx}^{2f} is proportional to the square of the relaxation time τ . The semiclassical treatment shows that such τ^2 contribution to the second-harmonic Hall current arises from energy shift due to orbital magnetic moment and the momentum shift related to chiral anomaly. These effects are substantially enhanced when the Fermi energy is close to the Weyl point reflecting the diverging Berry curvature around the Weyl point. Therefore, as shown in Figs. 4(c) and (d), large second-harmonic Hall and nonreciprocal magnetoresistance responses appear when the Fermi energy is tuned close to the Weyl points, which is qualitatively consistent with the observed enhancement of the second-harmonic Hall effect and the nonreciprocal magnetoresistance. In particular, when the Fermi energy is located between the Weyl and anti-Weyl points, the contribution from the two nodes

add up in a constructive way, leading to giant magnetochiral anisotropy.

Our theory can also explain the experimentally observed difference in the magnitudes of the second-harmonic Hall effect and the nonreciprocal magnetoresistance. As already shown in Figs. 1(d) and (e), the magnitude of the second-harmonic Hall effect is larger than that of the nonreciprocal magnetoresistance in sample F. Furthermore, all other samples also have the same relationship regardless of the current direction with respect to the crystalline axis; as presented in Figs. 4(a) and (b), the magnitude of the second-harmonic Hall effect is larger than that of the nonreciprocal magnetoresistance for each sample. In the theory, as can be seen from Eq. S11 [37], the second order current contains the $\mathbf{E} \cdot \mathbf{B}$ term that originates from the chiral anomaly [40, 41]. Since the $\mathbf{E} \cdot \mathbf{B}$ term is largest for $j // B$ (the second-harmonic Hall configuration) and zero for $j \perp B$ (the nonreciprocal magnetoresistance configuration), the second-harmonic Hall effect is always larger than the nonreciprocal magnetoresistance, if the Fermi level position is the same. Furthermore, the present theory is also consistent with the experimentally observed temperature dependence of ρ_{yx}^{2f}/ρ_{xx} and ρ_{xx}^{2f}/ρ_{xx} ; both ρ_{yx}^{2f}/ρ_{xx} and ρ_{xx}^{2f}/ρ_{xx} increase with decreasing temperature [see Figs. 3(b) and (c)]. Since the second-harmonic Hall effect and the nonreciprocal magnetoresistance in our theory are proportional to the square of the relaxation time, they should increase with decreasing temperature because of the enhancement of the relaxation time τ at low temperatures.

To summarize, we observed the giant magnetochiral anisotropy effect when the Fermi level is close to the Weyl points. A semiclassical calculation of magnetochiral anisotropy responses indicates that the diverging Berry curvature at the Weyl points plays a crucial role in the observed enhancement of the magnetochiral anisotropy. Our finding demonstrates that the Berry curvature has a large impact on the magnetochiral anisotropy effect and is important for exploring large diode effects.

Acknowledgments

This work was supported by JST FOREST Program (Grant No. JPMJFR203H), JST PRESTO (Grant No. JPMJPR19L9), JST CREST (Grant No. JPMJCR19T3), JSPS KAKENHI (Grant Nos. 22H04464, 22H05449, 21K18890, 21H01794, 19H05600, and 19K14667), and Murata Science Foundation

References

1. R. R. Birss, *Symmetry and Magnetism*. (North-Holland Pub., Amsterdam, 1966).
2. N. Nagaosa, J. Sinova, S. Okada, A. H. MacDonald, and N. P. Ong, Anomalous Hall effect. *Rev. Mod. Phys.* **82**, 1539 (2010).
3. Q. Ma *et al.*, Observation of the nonlinear Hall effect under time-reversal-symmetric conditions. *Nature* **565**, 337 (2019).
4. Z. Z. Du, H. Z. Lu, and X. C. Xie, Nonlinear Hall effects. *Nat. Rev. Phys.* **3**, 744 (2021).
5. I. Grinberg *et al.*, Perovskite oxides for visible-light-absorbing ferroelectric and photovoltaic materials. *Nature* **503**, 509 (2013).
6. G. B. Osterhoudt *et al.*, Colossal mid-infrared bulk photovoltaic effect in a type-I Weyl semimetal. *Nat. Mater.* **18**, 471 (2019).
7. Y. J. Zhang, T. Ideue, M. Onga, F. Qin, R. Suzuki, A. Zak, R. Tenne, J. H. Smet, and Y. Iwasa, Enhanced intrinsic photovoltaic effect in tungsten disulfide nanotubes. *Nature* **570**, 349 (2019).
8. D. Xiao, M.-C. Chang and Q. Niu, Berry phase effects on electronic properties. *Rev. Mod. Phys.* **82**, 1959 (2010).
9. S. Lai *et al.*, Third-order nonlinear Hall effect induced by the Berry-connection polarizability tensor. *Nat. Nanotech.* **16**, 869 (2021).
10. D. Kumar, C.-H. Hsu, R. Sharma, T.-R. Chang, P. Yu, J. Wang, G. Eda, G. Liang, and H. Yang, Room-temperature nonlinear Hall effect and wireless radiofrequency rectification in Weyl semimetal TaIrTe₄. *Nat. Nanotechnol.* **16**, 421 (2021).
11. S. M. Young and A. M. Rappe, First Principles Calculation of the Shift Current Photovoltaic Effect in Ferroelectrics. *Phys. Rev. Lett.* **109**, 116601 (2012).
12. T. Morimoto and N. Nagaosa, Topological nature of nonlinear optical effects in solids. *Sci. Adv.* **2**, e1501524 (2016).

13. Y. Tokura and N. Nagaosa, Nonreciprocal response from non-centrosymmetric quantum materials. *Nat. Commun.* **9**, 3740 (2018).
14. G. L. J. A. Rikken, J. Fölling and P. Wyder, Electrical Magnetochiral Anisotropy. *Phys Rev. Lett.* **87**, 236602 (2001).
15. F. Pop, P. Auban-Senzier, E. Canadell, G. L. J. A. Rikken, and N. Avarvari, Electrical magnetochiral anisotropy in a bulk chiral molecular conductor. *Nat. Commun.* **5**, 3757 (2014).
16. C. Avci, K. Garello, A. Ghosh, M. Gabureac, S. F. Alvarado, and P. Gambardella, Unidirectional spin Hall magnetoresistance in ferromagnet/normal metal bilayers. *Nat. Phys* **11**, 570 (2015).
17. T. Ideue, K. Hamamoto, S. Koshikawa, M. Ezawa, S. Shimizu, Y. Kaneko, Y. Tokura, N. Nagaosa, and Y. Iwasa, *Nat. Phys.* **13**, 578 (2017).
18. T. Yokouchi, N. Kanazawa, A. Kikkawa, D. Morikawa, K. Shibata, T. Arima, Y. Taguchi, F. Kagawa, and Y. Tokura, Electrical magnetochiral effect induced by chiral spin fluctuations. *Nat. Commun.* **8**, 866 (2017).
19. K. Yasuda, A. Tsukazaki, R. Yoshimi, K. Kondou, K. S. Takahashi, Y. Otani, M. Kawasaki, and Y. Tokura, Current-Nonlinear Hall Effect and Spin-Orbit Torque Magnetization Switching in a Magnetic Topological Insulator. *Phys. Rev. Lett.* **119**, 137204 (2017).
20. P. He, C.-H. Hsu, S. Shi, K. Cai, J. Wang, Q. Wang, G. Eda, H. Lin, V. M. Pereira, and H. Yang Nonlinear magnetotransport shaped by Fermi surface topology and convexity. *Nat. Commun.* **10**, 1290 (2019).
21. G. L. J. A. Rikken and N. Avarvari, Strong electrical magnetochiral anisotropy in tellurium. *Phys. Rev. B* **99**, 245153 (2019).
22. R. Aoki, Y. Kousaka, and Y. Togawa Anomalous Nonreciprocal Electrical Transport on Chiral Magnetic Order. *Phys. Rev. Lett.* **122**, 057206 (2019).
23. N. Jiang, Y. Nii, H. Arisawa, E. Saitoh, and Y. Onose, Electric current control of spin helicity in an itinerant helimagnet. *Nat. Commun.* **11**, 1601 (2020).
24. K. Yasuda, T. Morimoto, R. Yoshimi, M. Mogi, A. Tsukazaki, M. Kawamura, K. S. Takahashi, M. Kawasaki, N. Nagaosa, and Y. Tokura Large non-reciprocal charge transport mediated by quantum anomalous Hall edge states. *Nat. Nanotechnol.* **15**, 831 (2020).
25. F. Ando, Y. Miyasaka, T. Li, J. Ishizuka, T. Arakawa, Y. Shiota, T. Moriyama, Y. Yanase, and T. Ono, Observation of superconducting diode effect. *Nature* **584**, 373 (2020).

26. H. Narita *et al.*, Field-free superconducting diode effect in noncentrosymmetric superconductor/ferromagnet multilayers. *Nat. Nanotechnol.* **17**, 823 (2022).
27. F. Calavalle *et al.*, Gate-tuneable and chirality-dependent charge-to-spin conversion in tellurium nanowires. *Nat. Mater.* **21**, 526 (2022).
28. H. F. Legg *et al.*, Giant magnetochiral anisotropy from quantum-confined surface states of topological insulator nanowires. *Nat. Nanotechnol.* **17**, 696 (2022).
29. Y. Wang, H. F. Legg, T. Bömerich, J. Park, S. Biesenkamp, A. A. Taskin, M. Braden, A. Rosch, and Y. Ando, Gigantic Magnetochiral Anisotropy in the Topological Semimetal ZrTe₅. *Phys. Rev. Lett.* **128**, 176602 (2022).
30. L. Bauriedl *et al.*, Supercurrent diode effect and magnetochiral anisotropy in few-layer NbSe₂. *Nat. Commun.* **13**, 4266 (2022).
31. H. Ishizuka, and N. Nagaosa Anomalous electrical magnetochiral effect by chiral spin-cluster scattering. *Nat. Commun.* **11**, 2986 (2020).
32. N. P. Armitage, E. J. Mele, and A. Vishwanath, Weyl and Dirac semimetals in three-dimensional solids. *Rev. Mod. Phys.* **90**, 015001 (2018).
33. B. Q. Lv, T. Qian, and H. Ding, Experimental perspective on three-dimensional topological semimetals. *Rev. Mod. Phys.* **93**, 025002 (2021).
34. S. Kabashima, Electrical properties of tungsten-ditelluride WTe₂. *J. Phys. Soc. Jpn.* **21**, 945 (1966).
35. M. N. Ali *et al.*, Large, non-saturating magnetoresistance in WTe₂. *Nature* **514**, 205 (2014).
36. A. Soluyanov, D. Gresch, Z. Wang, Q.S. Wu, M. Troyer, X. Dai, and B. A. Bernevig, Type-II Weyl semimetals. *Nature* **527**, 495 (2015).
37. See the Supplemental Material for a description of the experimental method, theoretical calculations, and supplementary results.
38. Y. Y. Lv *et al.*, Experimental Observation of Anisotropic Adler-Bell-Jackiw Anomaly in Type-II Weyl Semimetal WTe_{1.98} Crystals at the Quasiclassical Regime. *Phys. Rev. Lett.* **118**, 096603 (2017).
39. T. Luo, H. Li, Y. M. Dai, H. Miao, Y. G. Shi, H. Ding, A. J. Taylor, D. A. Yarotski, R. P. Prasankumar, and J. D. Thompson, Hall effect in the extremely large magnetoresistance semimetal WTe₂. *Appl. Phys. Lett.* **107**, 182411 (2015).

40. J. Xiong, S. K. Kushwaha, T. Liang, J. W. Krizan, M. Hirschberger, W. Wang, R. J. Cava, and N. P. Ong, Evidence for the chiral anomaly in the Dirac semimetal Na_3Bi . *Science* **350**, 413 (2015).
41. M. Hirschberger, S. Kushwaha, Z. Wang, Q. Gibson, S. Liang, C. A. Belvin, B. A. Bernevig, R. J. Cava, and N. P. Ong, The chiral anomaly and thermopower of Weyl fermions in the half-Heusler GdPtBi . *Nat. Mater.* **15**, 1161 (2016).

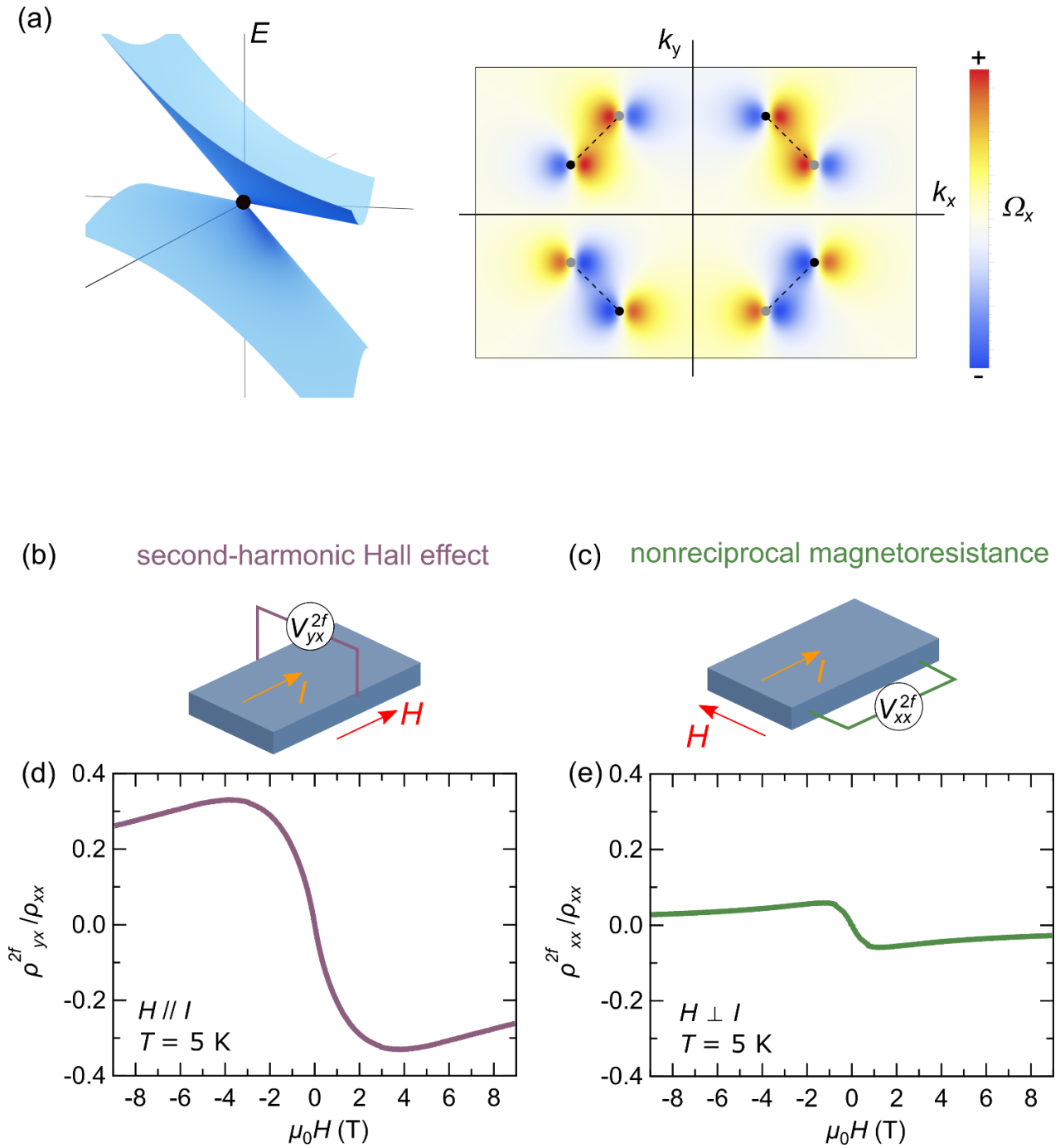


Fig. 1. (a) Schematics of the energy dispersion for a type-II Weyl semimetal near a Weyl point and the Berry curvature (Ω_x) around the Weyl points in WTe_2 . The black and grey circles represent Weyl points with the chirality $\eta = +1$ and -1 , respectively. Experimental configurations for (b) the second-harmonic Hall effect and (c) the nonreciprocal magnetoresistance. Magnetic-field dependence of (d) the second-harmonic Hall effect and (e) the nonreciprocal magnetoresistance in sample F measured with $j = 8.8 \times 10^5 \text{ Am}^{-2}$ and $f = 33 \text{ Hz}$ at 5 K . The current direction is parallel to the b -axis.

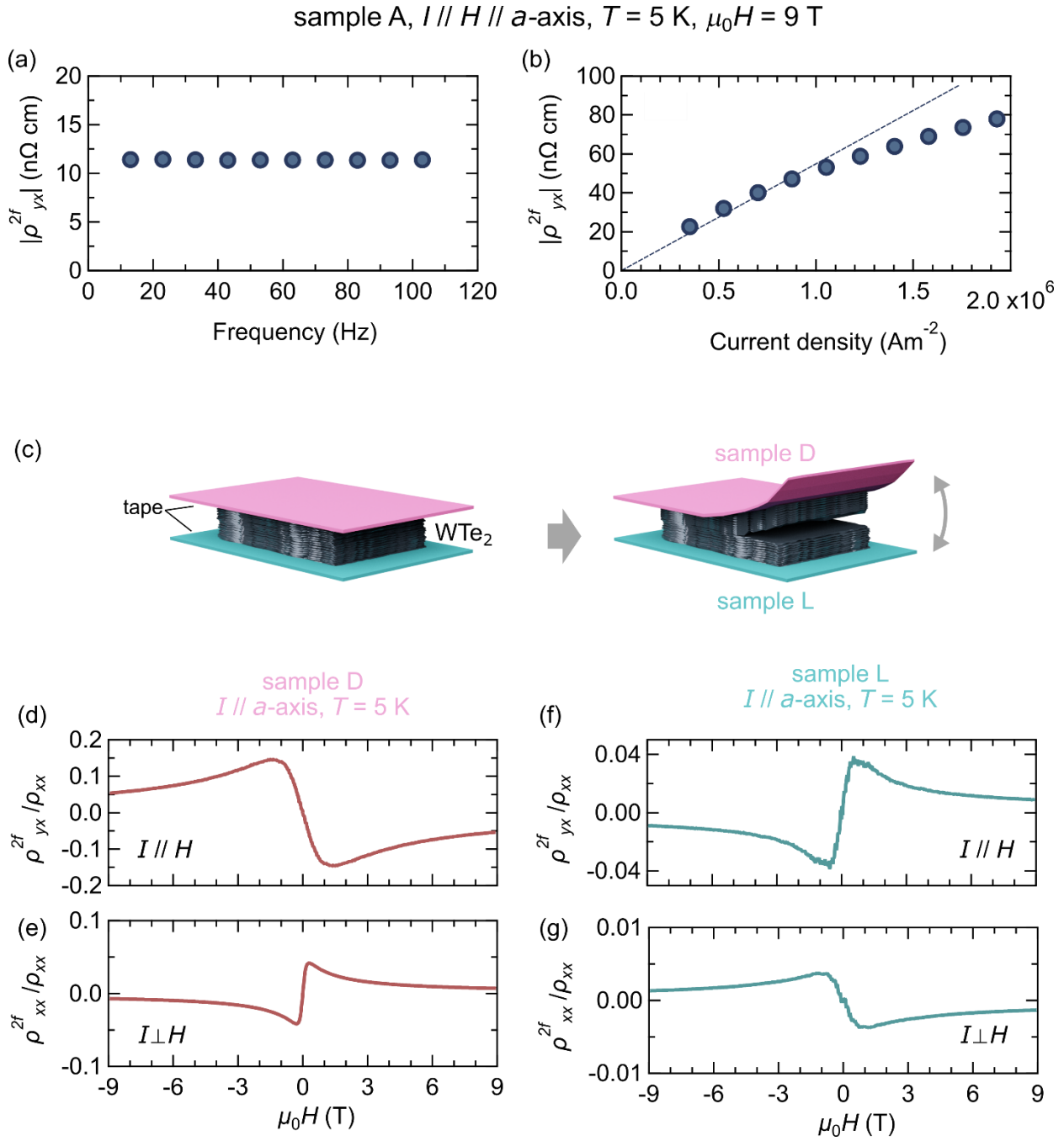


Fig. 2. (a) Frequency and (b) current density dependence of ρ_{yx}^{2f} in sample A. The frequency dependence is measured with $j = 4.4 \times 10^6 \text{ Am}^{-2}$ and the current dependence is measured with $f = 33$ Hz. The current direction is parallel to the a -axis. (c) Schematic of the fabrication of samples D and L, in which the polarity directions are opposite to each other. (d)-(g) Magnetic-field dependence of the second-harmonic Hall effect in sample D and sample L and the nonreciprocal magnetoresistance in sample D and sample L measured with $j = 1.2 \times 10^6 \text{ Am}^{-2}$ and $f = 33$ Hz.

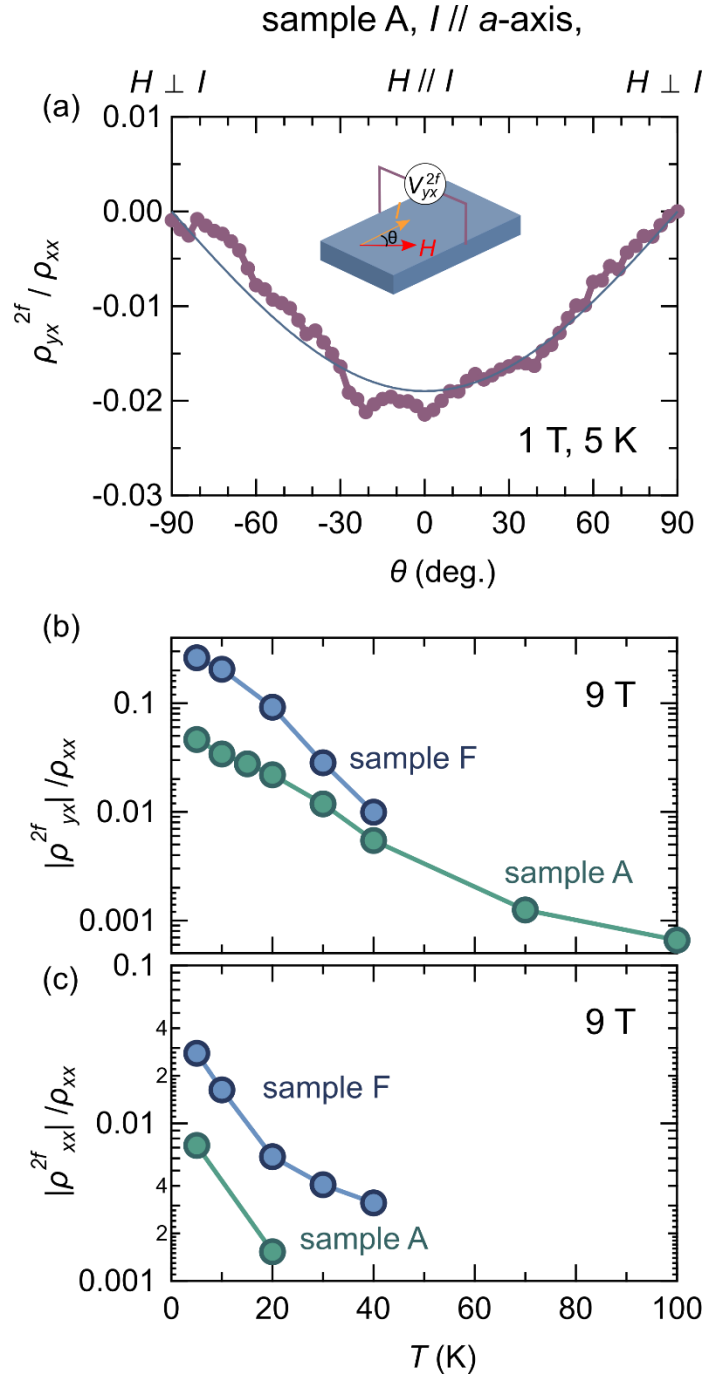


Fig. 3. (a) Angular dependence of ρ_{yx}^{2f}/ρ_{xx} measured with $j = 8.8 \times 10^5 \text{ Am}^{-2}$, $f = 3.3 \text{ Hz}$, and $I // a$ -axis. The definition of θ is shown in the inset. The blue lines are fits to $\cos \theta$. (b), (c) Temperature dependence of ρ_{yx}^{2f}/ρ_{xx} and ρ_{xx}^{2f}/ρ_{xx} at 9 T in samples A and F. The current density for sample A and sample F is $j = 8.8 \times 10^5 \text{ Am}^{-2}$ and $3.4 \times 10^5 \text{ Am}^{-2}$, respectively. The current direction is parallel to the a -axis in sample A and the b -axis in sample F. The frequency of the current is $f = 33 \text{ Hz}$ in both samples.

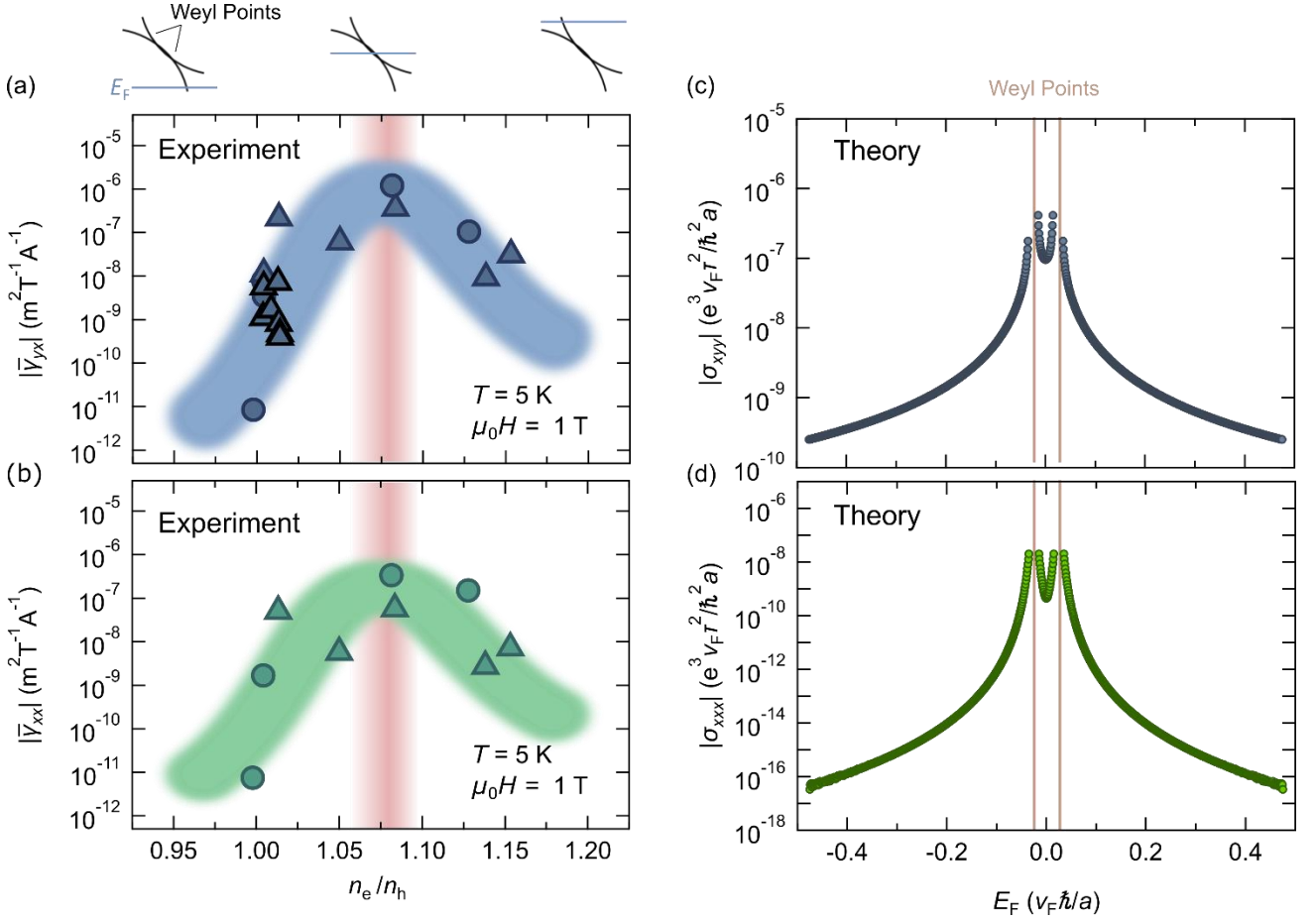


Fig. 4. (a), (b) Absolute values of $\bar{y}_{yx} = 2\rho_{yx}^{2f}/\rho_{xx} jB$ and $\bar{y}_{xx} = 2\rho_{xx}^{2f}/\rho_{xx} jB$ as a function of the ratio between electron carrier density (n_e) and hole carrier density (n_h). The circle and triangle points are samples measured with $I \parallel b$ -axis and $I \parallel a$ -axis, respectively. The upper panel schematically denotes the position of the Fermi level corresponding to the value of n_e/n_h . The region where the Fermi level is close to the Weyl points is denoted by the red shadow. The thick blue and green lines are a guide to the eyes. (c), (d) Absolute values of the second-harmonic Hall conductivity $\sigma_{xyy} = j_x/E_y^2$ and nonreciprocal magnetoresistance $\sigma_{xxx} = j_x/E_x^2$ as a function of the Fermi energy obtained from the semiclassical calculation. We set the magnetic field $B = 10^{-5} \hbar/ea^2$ and the energy separation of the two Weyl points $\Delta E = 0.05 v_F \hbar/a$.

Supplemental Material for
Giant Magnetochiral Anisotropy in Weyl-semimetal WTe₂ Induced by Diverging Berry Curvature

Tomoyuki Yokouchi¹, Yuya Ikeda², Takahiro Morimoto², and Yuki Shiomi¹

¹*Department of Basic Science, The University of Tokyo, Tokyo 152-8902, Japan*

²*Department of Applied Physics, The University of Tokyo, Tokyo 113-8656, Japan*

Symmetry consideration

The crystal structure of WTe₂ is orthorhombic with point group C_{2v} and this material has also time reversal symmetry T [S1]. Here we see what restrictions are imposed by such symmetries. The second-harmonic Hall effect can be represented as

$$j_x = \sigma_{xyy} E_y^2 B_y. \quad (\text{S1})$$

By performing the symmetry operator $C_{2T} = C_{2z}T$, E_y and B_y are transformed to $-E_y$ and B_y , respectively. Therefore, the nonreciprocal Hall current j_x must satisfy $j_x \rightarrow j_x$ under C_{2T} . In general, if we expand the current as $j = \sum_n j_n \tau^n$, where τ is the relaxation time, the expansion coefficients j_n are converted to $(-1)^{n+1} j_n$ under C_{2T} . Since j_0 is the normal Hall current, we can see that the second-harmonic Hall current is proportional to τ^2 at the lowest order.

The mirror symmetry in WTe₂ also constrains the direction of the nonreciprocal current response. For example, the nonreciprocal magnetoresistance (longitudinal nonreciprocal magneto-response) is not allowed when $B \parallel E$ where both B and E are normal to mirror plane (since the mirror operation leads to $J \rightarrow -J$, $E \rightarrow -E$ and $B \rightarrow B$). In contrast, the nonreciprocal magnetoresistance is allowed when $B \perp E$, which can be represented as

$$j_x = \sigma_{xx} E_x^2 B_y. \quad (\text{S2})$$

From the same argument as above, the nonreciprocal magnetoresistance is proportional to τ^2 at the lowest order.

Formalism of semiclassical calculation

We use Boltzmann equation to derive momentum distribution under the electric field and the magnetic field and calculate the nonlinear current response. The semiclassical equation of motion for an electron under the electric field and the magnetic field are [S2, S3]

$$\dot{\mathbf{r}} = \frac{1}{\hbar D} \left[\nabla_{\mathbf{k}} \epsilon_{\mathbf{k}} + e \mathbf{E} \times \boldsymbol{\Omega}_{\mathbf{k}} + \frac{e}{\hbar} (\nabla_{\mathbf{k}} \epsilon_{\mathbf{k}} \cdot \boldsymbol{\Omega}_{\mathbf{k}}) \mathbf{B} \right] \quad (\text{S3})$$

$$\hbar \dot{\mathbf{k}} = \left[-e \mathbf{E} - \frac{e}{\hbar} \nabla_{\mathbf{k}} \epsilon_{\mathbf{k}} \times \mathbf{B} - \frac{e^2}{\hbar} (\mathbf{E} \cdot \mathbf{B}) \boldsymbol{\Omega}_{\mathbf{k}} \right] \quad (\text{S4})$$

$$D = 1 + \frac{e}{\hbar} \mathbf{B} \cdot \boldsymbol{\Omega}_{\mathbf{k}}. \quad (\text{S5})$$

The third term in $\dot{\mathbf{k}}$ describe the momentum shift due to the chiral anomaly within semiclassical approach. The energy dispersion $\epsilon_{\mathbf{k}}$ includes correction due to magnetic orbital moment,

$$\epsilon_{\mathbf{k}} = \epsilon_{\mathbf{k}}^0 - \mathbf{m}_{\mathbf{k}} \cdot \mathbf{B}. \quad (\text{S6})$$

In the uniform system, current density \mathbf{j} is given by

$$\mathbf{j} = -e \int [d\mathbf{k}] D \dot{\mathbf{r}} f, \quad (\text{S7})$$

where f is the distribution function and we define $[d\mathbf{k}] \equiv d\mathbf{k}/(2\pi)^3$.

Now, we expand the distribution function with respect to \mathbf{E} as

$$f = f_0 + f_1 + f_2, \quad (\text{S8})$$

where $f_0 = \theta(E_{\text{F}} - \epsilon_{\mathbf{k}}^0 + \mathbf{m}_{\mathbf{k}} \cdot \mathbf{B})$ is the unperturbed distribution function. The steady state is determined by the Boltzmann equation with relaxation time approximation

$$\frac{df}{dt} = \dot{\mathbf{k}} \cdot \nabla_{\mathbf{k}} f = \frac{f_0 - f}{\tau}. \quad (\text{S9})$$

The second-order response proportional to τ^2 is obtained from f_2 . Substituting Eq. (S8) successively into Eq. (S9), f_2 is given by

$$f_2 = \left\{ \frac{e\tau}{\hbar D} \left[\mathbf{E} + \frac{e}{\hbar} (\mathbf{E} \cdot \mathbf{B}) \boldsymbol{\Omega}_{\mathbf{k}} \right] \cdot \nabla_{\mathbf{k}} \right\}^2 f_0, \quad (\text{S10})$$

where we have dropped the term involving $\nabla_{\mathbf{k}} \epsilon_{\mathbf{k}} \times \mathbf{B}$ because this term is perpendicular to $\nabla_{\mathbf{k}} f_i = (\nabla_{\mathbf{k}} \epsilon_{\mathbf{k}}) \partial_{\epsilon} f_i$ ($i = 0, 1$). The second-order current response (of the frequency 2ω) is obtained as

$$\begin{aligned} \mathbf{j}_2 &= -e \int [d\mathbf{k}] D \dot{\mathbf{r}} f_2 \\ &= -\tau^2 \frac{e^3}{\hbar^2} \int [d\mathbf{k}] \left[\mathbf{v}_{\mathbf{k}} + \frac{e}{\hbar} (\mathbf{v}_{\mathbf{k}} \cdot \boldsymbol{\Omega}_{\mathbf{k}}) \mathbf{B} \right] \left\{ \frac{e\tau}{\hbar D} \left[\mathbf{E} + \frac{e}{\hbar} (\mathbf{E} \cdot \mathbf{B}) \boldsymbol{\Omega}_{\mathbf{k}} \right] \cdot \nabla_{\mathbf{k}} \right\}^2 f_0, \end{aligned} \quad (\text{S11})$$

with $\mathbf{v}_k = (1/\hbar)\nabla_k \epsilon_k$. Now we focus on the second-harmonic Hall current $j_x = \sigma_{xyy} E_y^2 B_y$ and thus drop the term involving $(\mathbf{v}_k \cdot \boldsymbol{\Omega}_k) \mathbf{B}$. Integrating by parts leads to

$$\begin{aligned}
j_x &= \tau^2 \frac{e^3}{\hbar^2} E_y^2 \int_{\text{BZ}} [d\mathbf{k}] \frac{1}{D} \left(\frac{\partial(v_k^x/D)}{\partial k_y} + \frac{e}{\hbar} B_y \nabla_k \cdot (v_k^x \boldsymbol{\Omega}_k/D) \right) \left[\mathbf{e}_y + \frac{e}{\hbar} B_y \boldsymbol{\Omega}_k \right] \cdot \nabla_k f_0 \\
&= \tau^2 \frac{e^3}{\hbar^2} E_y^2 \int_{\text{BZ}} [d\mathbf{k}] \frac{1}{D} \left(\frac{\partial(v_k^x/D)}{\partial k_y} + \frac{e}{\hbar} B_y \nabla_k \cdot (v_k^x \boldsymbol{\Omega}_k/D) \right) \left[v_k^y + \frac{e}{\hbar} B_y \mathbf{v}_k \cdot \boldsymbol{\Omega}_k \right] \frac{\partial f_0}{\partial \epsilon} \\
&= \tau^2 \frac{e^3}{\hbar^2} E_y^2 \int_S [d\mathbf{k}] \frac{1}{D|\mathbf{v}_k|} \left(\frac{\partial(v_k^x/D)}{\partial k_y} + \frac{e}{\hbar} B_y \nabla_k \cdot (v_k^x \boldsymbol{\Omega}_k/D) \right) \left[v_k^y + \frac{e}{\hbar} B_y \mathbf{v}_k \cdot \boldsymbol{\Omega}_k \right]. \quad (\text{S12})
\end{aligned}$$

In the third line, the range of integration is changed to the Fermi surface S because $\partial_\epsilon f_0 = \delta(E_F - \epsilon)$. The second-harmonic Hall conductivity shows a rapid enhancement around the Weyl points reflecting the diverging Berry curvature. We note that the second-harmonic Hall response from the Berry curvature dipole mechanism arises from f_1 , which is in the linear order in τ and is prohibited in the present setup by C_{2T} symmetry for WTe_2 .

From Eq. (S11), we can also obtain the formula for the nonreciprocal magnetoresistance $j_x = \sigma_{xxx} E_x^2 B_y$. Since \mathbf{B} and \mathbf{E} are perpendicular, we can drop the chiral anomaly terms involving $(\mathbf{E} \cdot \mathbf{B})$ in the distribution function under the electromagnetic field, which leads to

$$\begin{aligned}
j_x &= \tau^2 \frac{e^3}{\hbar^2} E_x^2 \int_{\text{BZ}} [d\mathbf{k}] \frac{1}{D} \frac{\partial(v_k^x/D)}{\partial k_x} \frac{\partial f_0}{\partial k_x} \\
&= \tau^2 \frac{e^3}{\hbar^2} E_x^2 \int_S [d\mathbf{k}] \frac{v_k^x}{D|\mathbf{v}_k|} \frac{\partial(v_k^x/D)}{\partial k_x}. \quad (\text{S13})
\end{aligned}$$

This nonreciprocal current response is nonzero due to the orbital magnetic moment. However, as discussed in the main text, the second-harmonic Hall response includes not only the orbital magnetic moment effect but also the chiral anomaly effect $(\mathbf{E} \cdot \mathbf{B})$, so the magnitude of the second-harmonic Hall effect is larger than the nonreciprocal magnetoresistance.

Second-harmonic Hall conductivity of tilted Weyl semimetals

We consider the Weyl Hamiltonian with a tilt,

$$H = \eta v_F \mathbf{k} \cdot \boldsymbol{\sigma} + v_t k_t \sigma_0, \quad (\text{S14})$$

where $k_t = k_x \cos \theta_t + k_y \sin \theta_t$ is the direction of tilt and $\eta = \pm 1$ specifies the chirality. The energy dispersion is given by

$$\epsilon_{\mathbf{k}}^{\pm} = \pm v_F k + v_t k_t - \mathbf{m}_{\mathbf{k}} \cdot \mathbf{B}, \quad (\text{S15})$$

which is linear in k . For the above the Hamiltonian, the Berry curvature and the orbital magnetic moment are written as

$$\boldsymbol{\Omega}_{\mathbf{k}}^{\pm} = \mp \eta \frac{\mathbf{k}}{2k^3}, \quad (\text{S16})$$

$$\mathbf{m}_{\mathbf{k}} = -\eta \frac{\mathbf{k}}{2k^2}. \quad (\text{S17})$$

WTe₂ host 4 pairs of Weyl and anti-Weyl fermions which are connected with mirror symmetries along the x and y directions as shown in Fig. S1(a). Explicitly, four Weyl points with the tilt angle and the chirality $(\theta_t, \eta), (-\theta_t, -\eta), (\pi + \theta_t, \eta), (\pi - \theta_t, -\eta)$ are connected with mirror symmetries. In the magnetic field, the Fermi surface of each Weyl point shifts due to the orbital magnetization as illustrated in Fig. S1(b). Using Eq. (S12), the second-harmonic Hall conductivity is computed for these four pairs of Weyl fermions as shown in Fig. S1(c). Due to the divergence of the Berry curvature at each of the Weyl points at different energies, the second-harmonic Hall conductivity shows a rapid enhancement around the Weyl points. In particular, when the Fermi energy is located between the two Weyl nodes, the contributions from the two Weyl nodes add up, leading to a large second-harmonic Hall effect shown as Figure 4(c) in the main text. We note that, in this calculation, the integration is performed only on the Fermi surfaces that change continuously from the ones in the absence of the magnetic field. The magnetic field dependence of the second-harmonic Hall conductivity is also calculated as shown in Fig. S1(d). Only B -odd terms are allowed due to C_2 symmetry along the z direction. We see that the conductivity is B -linear in the small magnetic field region, which corresponds to the nonreciprocal second-harmonic Hall current in Eq. (S1). These results show that the experimentally observed Fermi-level dependence can be explained by a semiclassical calculation of nonreciprocal responses which incorporates the effect of energy shift due to the orbital magnetic moment and momentum shift induced by the chiral anomaly of Weyl fermions.

We note that the unit of the energy in Fig. 1 is given by $[v_F \hbar / a]$. For typical parameters for Weyl semimetals, $v_F = 10^5 \text{ m/s}$ and $a = 3 \text{ \AA}$, this energy unit amounts to $v_F \hbar / a \simeq 0.2 \text{ eV}$, where the Weyl node separation of $\Delta E = 0.05 v_F \hbar / a \simeq 0.01 \text{ eV}$ that is used for Fig. S1(c) becomes comparable with that for WTe₂ [S1].

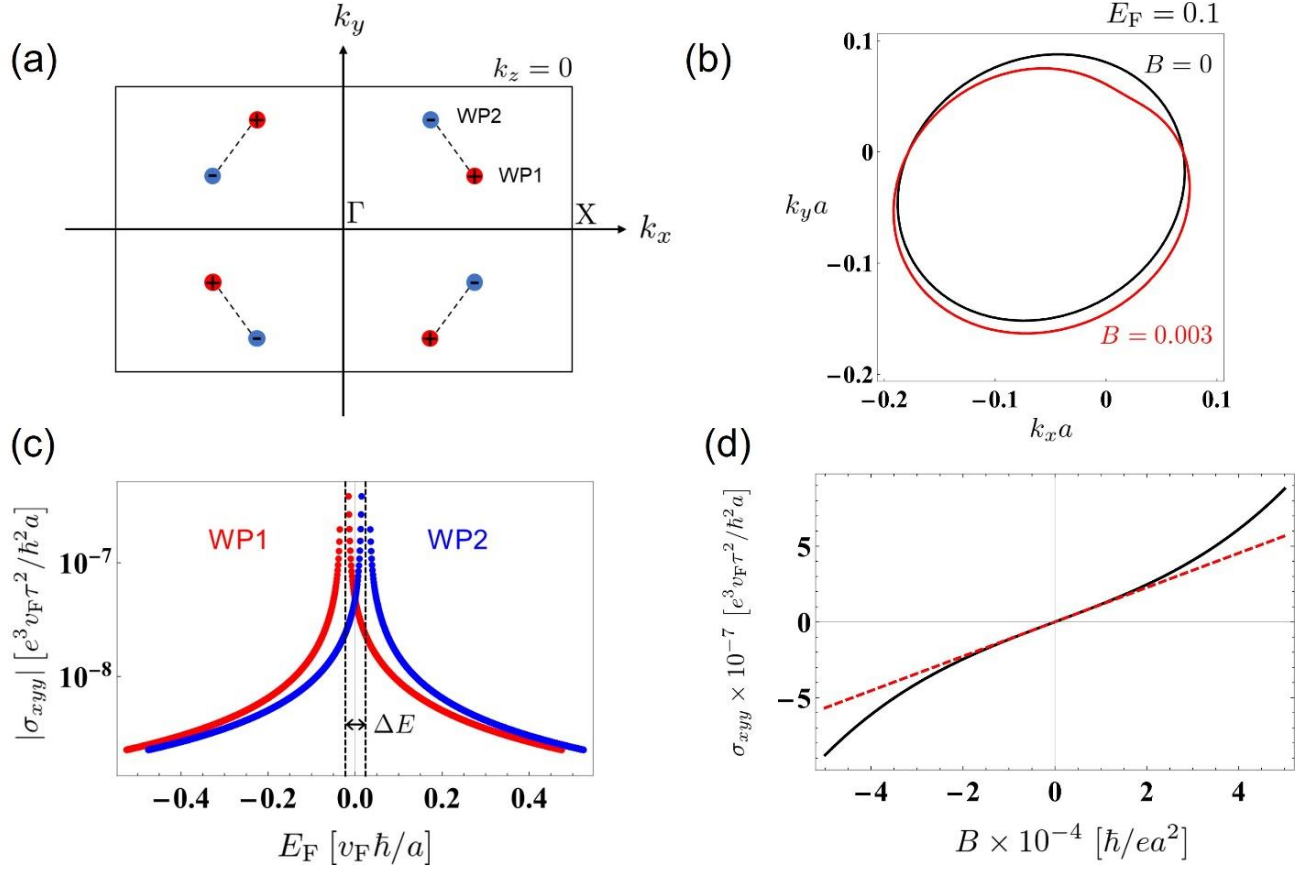


Fig. S1. Theoretical calculation of second-harmonic Hall conductivity of tilted Weyl fermions.

(a) Schematic picture of four pairs of Weyl and anti-Weyl points in WTe_2 , where their chirality is marked with red ($\eta = 1$) and blue ($\eta = -1$). The four Weyl pairs appear at the $k_z = 0$ plane in a way satisfying the mirror symmetries along x and y directions. (b) Cross-section of Fermi surface at the $k_z = 0$ plane in the absence (black line) and the presence (red line) of the magnetic field B . In the presence of magnetic field in the y direction, the Fermi surface shifts down in the k_y direction due to the orbital magnetization. (E_F and B are expressed in a dimensionless unit with $e = \hbar = a = 1$ for simplicity.) (c) The Fermi level dependence of the second-harmonic Hall conductivity of two Weyl points with energy $\pm \Delta E / 2$. We set the magnetic field $B = 10^{-5} \hbar / ea^2$ and the Weyl node separation $\Delta E = 0.05 v_F \hbar / a$. The second-harmonic Hall conductivity shows a rapid enhancement around the Weyl points reflecting the diverging Berry curvature. (d) The magnetic field dependence of the second-harmonic Hall conductivity (black line). The conductivity is B -odd and, in the small field region, is B -linear (the red line is linear-fitting). We used the parameters, $v_t / v_F = 0.5$, $\theta_t = \pi / 3$.

Sample preparation

Single crystals of WTe_2 were synthesized by a self-flux method [S4]. First, the mixture of high-purity W and Te powders was heated up to 835 °C in an evacuated quartz tube. Next, the tube was cooled down to 535 °C at the rate of 2 °C/hour. Then, Te was removed by centrifuging. Finally, we annealed the crystals at 415 °C in an evacuated quartz tube for several days.

The typical size of obtained samples is $2 \times 0.3 \times 0.04 \text{ mm}^3$. In Fig. S2 and S3, we show the temperature dependence of the resistivity and the magnetoresistance, both of which are consistent with the previous report [S5].

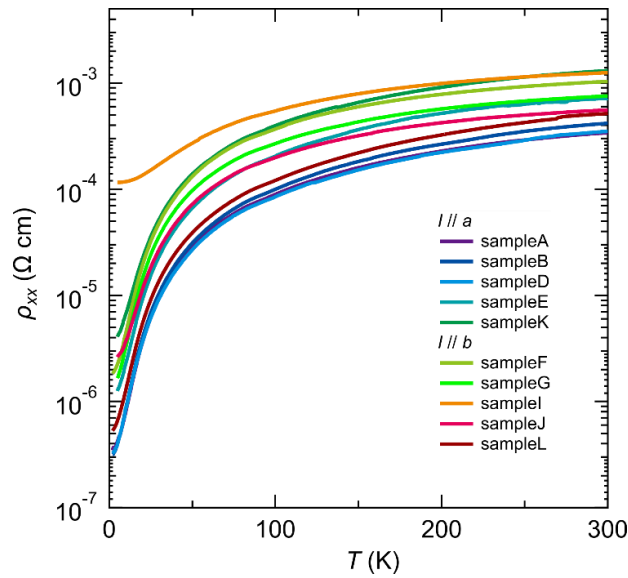


Fig. S2. Temperature dependence of longitudinal resistivity for sample A to sample L.

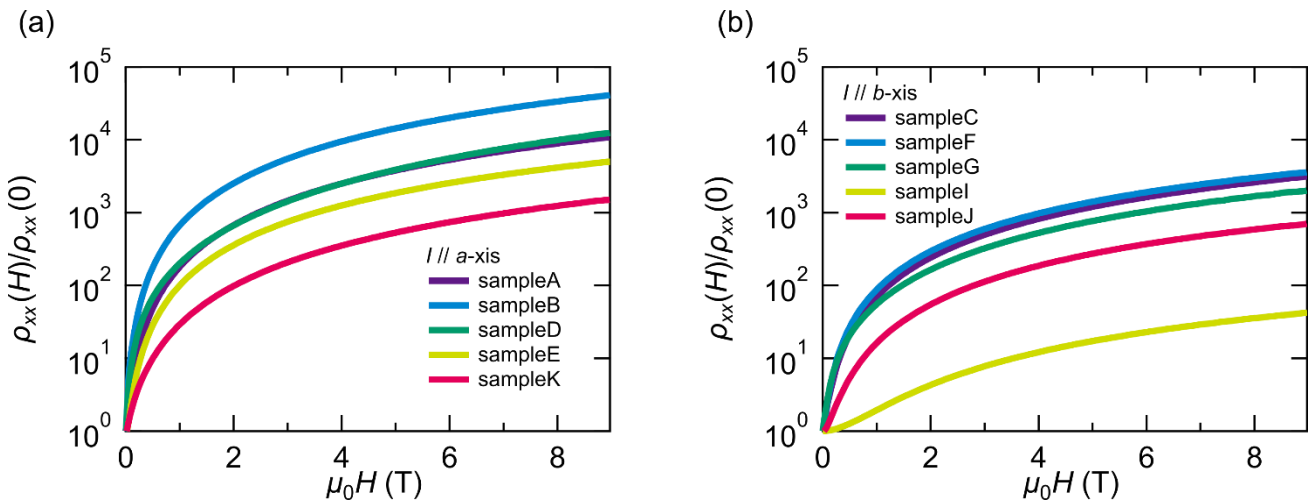


Fig. S3. Magnetic field dependence of longitudinal resistivity for samples with $I // a$ -axis (a) and with $I // b$ -axis (b) at 5 K. The magnetic field is applied parallel to the c -axis.

Transport measurements

We connected gold wires to WTe₂ single crystals with silver paste (Dupont 4922 or Epo-Tek H20E). The electrode distances and the thickness of the samples were measured with a laser microscope (Keyence VK-9500). Temperature and magnetic-field dependence of longitudinal resistivity and Hall resistivity (Figs. S2-S4) were measured by using dc-transport option of Physical Property Measurement System (PPMS).

Second harmonic resistivity was measured by using a lock-in technique (NF LI5650) and AC current source (Lake Shore 155); we input low-frequency (f) ac current and measured second harmonic voltage. The second harmonic longitudinal and transverse resistivities (ρ_{xx}^{2f} and ρ_{yx}^{2f}) are defined as $\rho_{xx}^{2f} = V_{xx}^{2f} S/Id$ and $\rho_{yx}^{2f} = V_{yx}^{2f} S/Id$, respectively. Here, S , I , d , V_{xx}^{2f} , and V_{yx}^{2f} are cross-section area of WTe₂, the current, the distance between voltage terminal, the longitudinal second harmonic voltage, and the transverse second harmonic voltage, respectively. Here, ρ_{xx}^{2f} and ρ_{yx}^{2f} were anti-symmetrized against the magnetic field as follows: $\rho_{xx}^{2f}(H) = [\rho_{xx,\text{meas.}}^{2f}(H) - \rho_{xx,\text{meas.}}^{2f}(-H)]/2$ and $\rho_{yx}^{2f}(H) = [\rho_{yx,\text{meas.}}^{2f}(H) - \rho_{yx,\text{meas.}}^{2f}(-H)]/2$, where $\rho_{xx,\text{meas.}}^{2f}(H)$ and $\rho_{yx,\text{meas.}}^{2f}(H)$ are the measured second harmonic longitudinal and transverse resistivities, respectively. We show $\rho_{xx,\text{meas.}}^{2f}(H)$ and $\rho_{yx,\text{meas.}}^{2f}(H)$ for sample F in Fig. S5; the antisymmetric component is dominant in $\rho_{xx,\text{meas.}}^{2f}(H)$ and $\rho_{yx,\text{meas.}}^{2f}(H)$. In the calculation of ρ_{xx}^{2f}/ρ_{xx} and ρ_{yx}^{2f}/ρ_{xx} , ρ_{xx} simultaneously measured together with ρ_{xx}^{2f} or ρ_{yx}^{2f} with a lock-in amplifier is used. The figures of merit of the second-harmonic Hall effect $\bar{\gamma}_{yx}$ and nonreciprocal magnetoresistance $\bar{\gamma}_{xx}$ are defined as $\bar{\gamma}_{yx} = 2\rho_{yx}^{2f}/(\rho_{xx}jB)$ and $\bar{\gamma}_{xx} = 2\rho_{xx}^{2f}/(\rho_{xx}jB)$, where j is the current density [S6]. We show ρ_{xx} , ρ_{yx}^{2f} , ρ_{yx}^{2f}/ρ_{xx} , ρ_{xx}^{2f} , ρ_{xx}^{2f}/ρ_{xx} for all samples in Fig. S6 and Fig. S7. In the measurement of the angular dependence [Fig. 3(a) in the main text], we anti-symmetrized ρ_{yx}^{2f} with respect to the magnetic field as well as the angle as follows:
$$\rho_{yx}^{2f}(\theta) = \frac{\{[(\rho_{yx,\text{meas.}}^{2f}(\theta, H) - \rho_{yx,\text{meas.}}^{2f}(\theta, -H))] - [\rho_{yx,\text{meas.}}^{2f}(\theta + \pi, H) - \rho_{yx,\text{meas.}}^{2f}(\theta + \pi, -H)]\}}{4}.$$

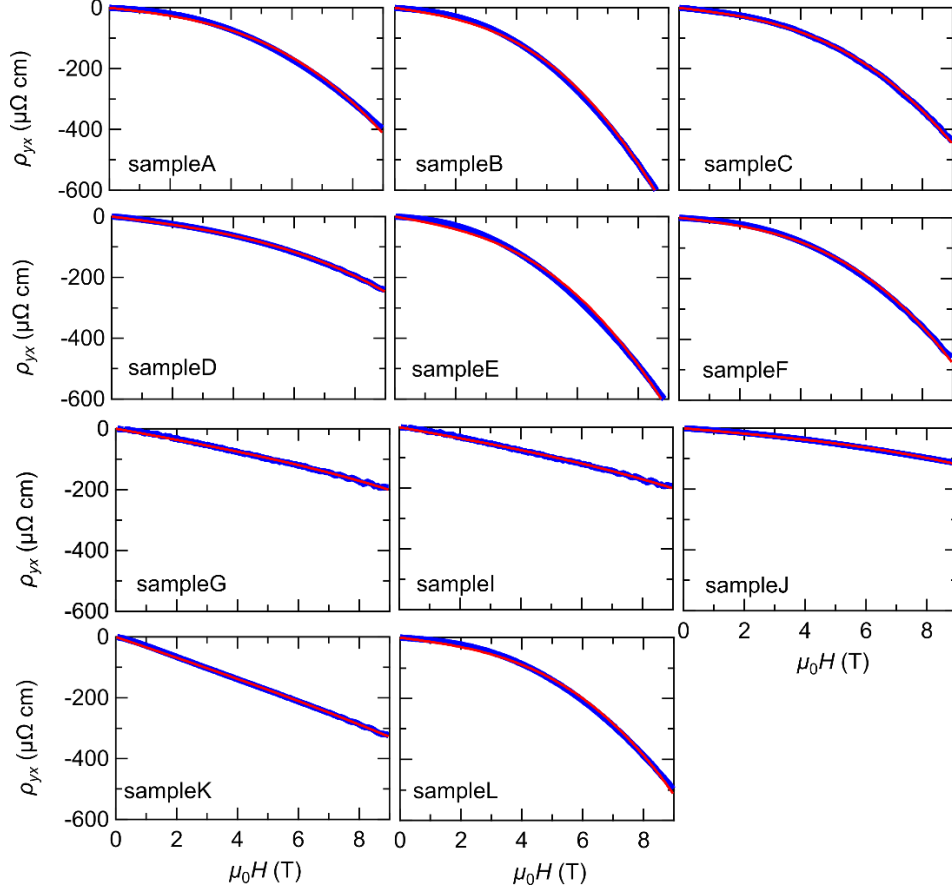


Fig. S4. Magnetic field dependence of Hall resistivity at 5 K. The blue curves show the measured Hall resistivity, and the red curves are fitting curves with the two-carrier model [Eq. (1) in the main text]. The magnetic field is applied parallel to the c -axis.

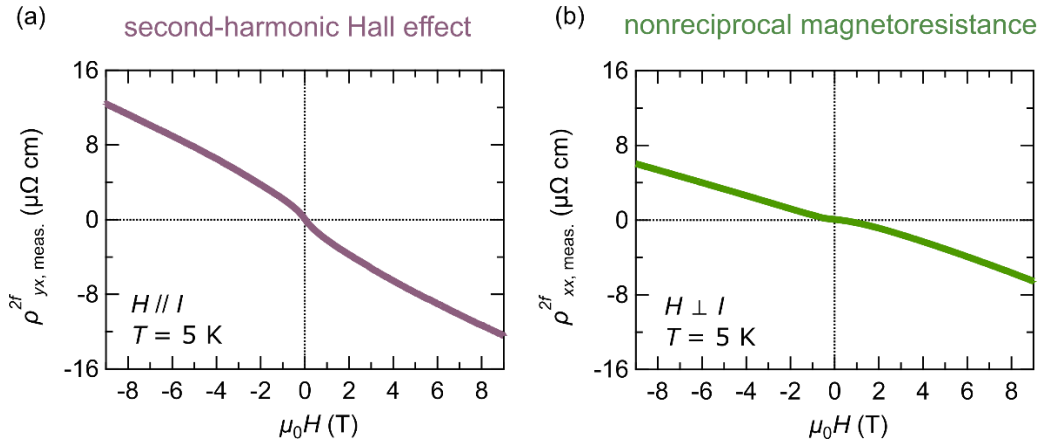


Fig. S5. Magnetic-field dependence of the raw data of second-harmonic Hall effect (a) and the nonreciprocal magnetoresistance (b) in sample F measured with $j = 8.8 \times 10^5 \text{ Am}^{-2}$ and $f = 33 \text{ Hz}$ at 5 K. The current direction is parallel to the b -axis. The corresponding anti-symmetrized data normalized by ρ_{xx} is shown in Fig. 1 in the main text.

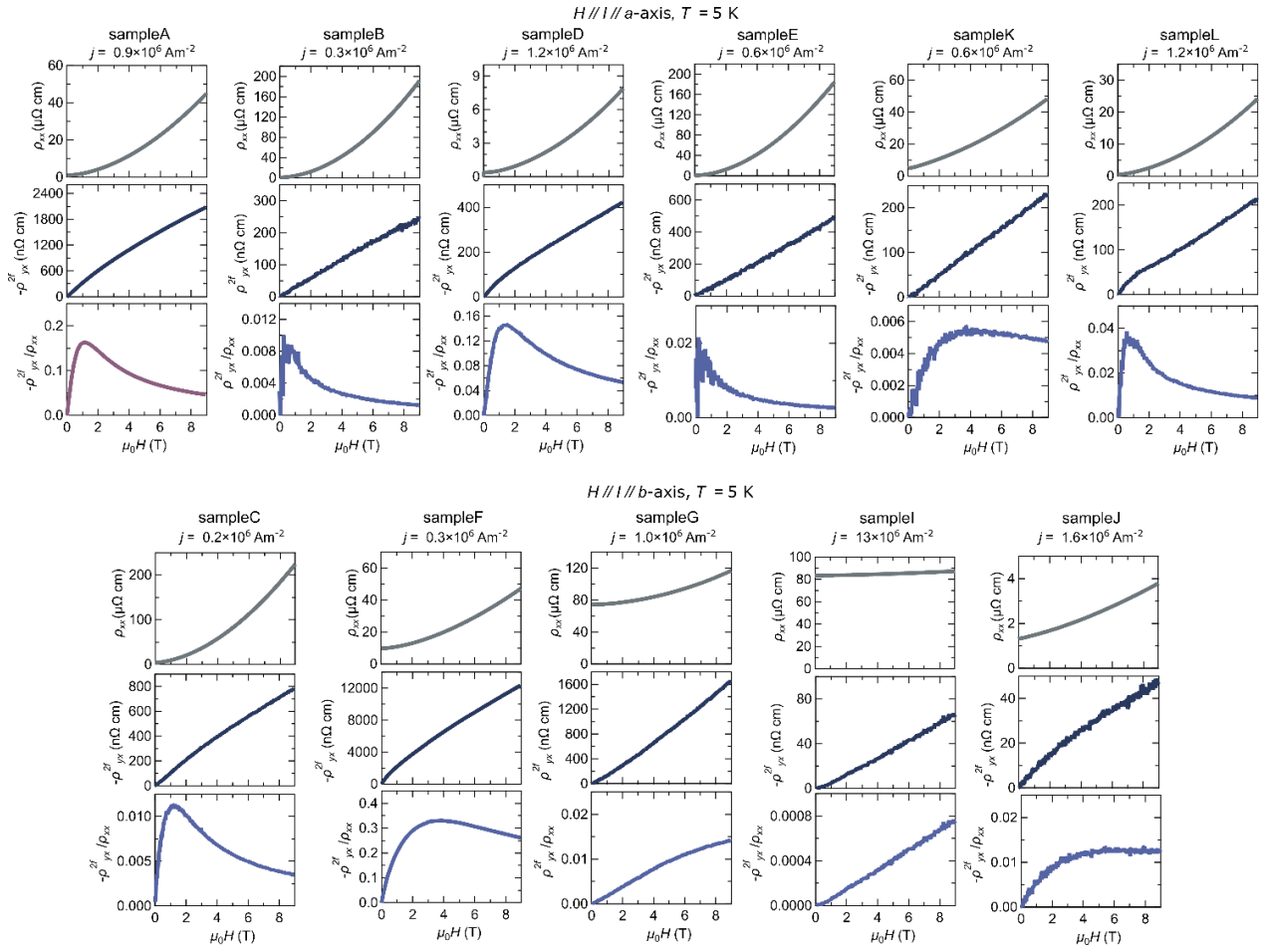


Fig. S6. Magnetic field dependence of longitudinal resistivity, second-harmonic Hall resistivity, and second-harmonic Hall resistivity normalized by the longitudinal resistivity measured with $H // I$ at 5 K.

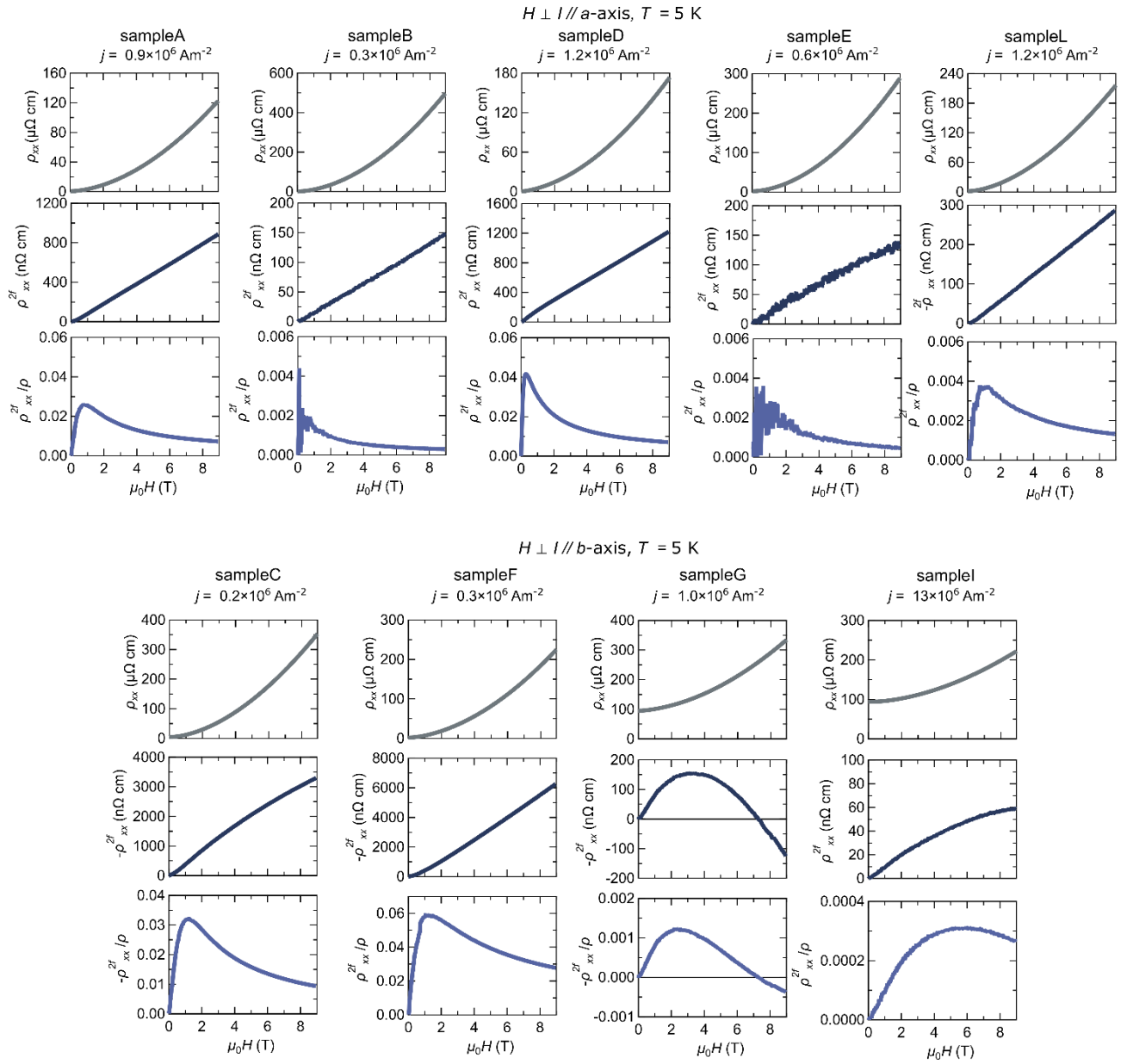


Fig. S7. Magnetic field dependence of longitudinal resistivity, nonreciprocal magnetoresistance, and nonreciprocal magnetoresistance normalized by the longitudinal resistivity ρ_{xx} measured with $H \perp I$ at 5 K.

Evaluation of hole and electron carrier densities

The hole and electron carrier densities (n_h and n_e) are determined by adopting a two-band model with one-electron band and one-hole band as follows [S8]:

$$\rho_{yx} = \frac{(n_h \mu_h^2 - n_e \mu_e^2) + (n_h - n_e) \mu_h^2 \mu_e^2}{(n_h \mu_h + n_e \mu_e)^2 + (n_h - n_e)^2 \mu_h^2 \mu_e^2 B^2} \frac{B}{e}, \quad (\text{S18})$$

where $n_h, n_e, \mu_h, \mu_e, e$ are hole carrier density, electron carrier density, hole mobility, electron mobility, and elementary charge, respectively. In Fig. S4, we show the magnetic-field dependence of Hall resistivity and fitting curves with Eq. (S18). The Hall resistivity is well fitted with the two-band model.

In bulk WTe₂, the carrier density is controlled by annealing because of a change in the Te composition [S9]. In sample K, we repeated the transport measurement and the annealing to vary the Te composition. Each annealing was performed at 150 °C for approximately 1 hour in a vacuum. We performed the annealing and the measurement of the second-harmonic Hall effect seven times in sample K. After the repeated experiments, n_h/n_e changes by 0.97 %, eventually.

References for Supplementary Materials

- [S1] A. Soluyanov, *et al.*, Type-II Weyl Semimetals. *Nature* **527**, 495 (2015).
- [S2] A. Zyuzin, *et al.*, Chiral anomaly and second-harmonic generation in Weyl semimetals. *Phys. Rev. B* **95**, 085127 (2017).
- [S3] T. Morimoto, *et al.*, Semiclassical theory of nonlinear magneto-optical responses with applications to topological Dirac/Weyl semimetals. *Phys. Rev. B* **94**, 245121 (2016).
- [S4] M. N. Ali *et al.*, Correlation of crystal quality and extreme magnetoresistance of WTe₂ *EPL* **110**, 67002 (2015).
- [S5] M. N. Ali *et al.*, Large, non-saturating magnetoresistance in WTe₂. *Nature* **514**, 205 (2014).
- [S6] Y. Tokura and N. Nagaosa, Nonreciprocal response from non-centrosymmetric quantum materials. *Nat. Commun.* **9**, 3740 (2018).
- [S7] T. Luo *et al.*, Hall effect in the extremely large magnetoresistance semimetal WTe₂. *Appl. Phys. Lett.* **107**, 182411 (2015).
- [S8] Y. Y. Lv *et al.*, Experimental Observation of Anisotropic Adler-Bell-Jackiw Anomaly in Type-II Weyl Semimetal Wte_{1.98} Crystals at the Quasiclassical Regime. *Phys. Rev. Lett.* **118**, 096603 (2017).